An Improved MPC With Reduced CMV and Current Distortion for PMSM Drives Under Variable DC-Bus Voltage Condition in Electric Vehicles

Jiayao Li, *Student Member, IEEE*, Wensheng Song, *Senior Member, IEEE*, Hao Yue, *Student Member, IEEE*, Na Sun, Chenwei Ma, *Member, IEEE*, and Rong Feng

***Abstract*—The conventional reduced-common-mode-voltage model predictive control (RCMV-MPC) faces the challenges of low control accuracy and high switching frequency at low speeds. To reduce CMV, improve steady-state performance and lower switching frequency, an improved MPC is proposed for permanent magnet synchronous motor (PMSM) drives with variable dc-bus voltage in electric vehicles (EVs). First, the virtual vectors with low CMV and switching frequency are defined, the optimal virtual vector and its duty cycle are determined. Then, the limitation of designed virtual vectors with fixed dc-bus voltage is illustrated. Furthermore, based on the analysis of the effect of dc-bus voltage on current distortion, the optimal reference dc-bus voltage is adopted to minimize the current distortion. At last, the dc-bus voltage is adjusted to track the reference value by dc–dc converter. An experimental comparison of the conventional methods and the proposed scheme is carried out. The results have verified that the proposed scheme can reduce CMV, current harmonics and switching frequency, especially in low-speed regions. As dc–dc converter has become more popular in motor drives of EVs, the proposed scheme could have a promising application perspective.**

***Index Terms*—Common-mode voltage (CMV), current distortion, model predicted control (MPC), permanent magnet synchronous motors (PMSMs).**

I. Introduction

DUE to several salient advantages, such as small size, light weight and high power density, permanent magnet synchronous motors (PMSMs) have been widely employed in motor drive systems [1], [2]. With the rapid development of modern control theory and digital controllers, great attention has been attracted to model predictive control (MPC) for decades because of its fast dynamic response, simple control structure and ease of handling nonlinear constraints [3], [4], [5]. According to different control variables, the finite-control-set MPC (FCS-MPC) methods applied to PMSMs are mainly composed of model predictive current control (MPCC) [6] and model predictive torque control [7]. Among them, MPCC is easier to implement in practical applications without weighting factor adjustments because the control variables are both currents [8].

The FCS-MPC is simple and intuitive to implement for constrained nonlinear systems and can consider the discrete nature of the power converter. In [6], eight discrete voltage vectors are acted on the inverter to realize MPCC. However, the current and torque ripples are relatively large for only single vector acts during one sampling interval. Therefore, the MPC with duty cycle control is proposed to improve the steady-state performance [9]. To reduce the current harmonics further, multi-vector MPC methods are proposed in [10], [11]. However, the computational burden increases significantly as the number of vector combinations increases. To release the computational burden, deadbeat MPC (DB-MPC) methods are proposed in [12], [13]. Thereby, better steady-state performance and lower computational burden are obtained.

Regardless of which MPC method is employed, the vectors that generate large common-mode voltage (CMV) will be used inevitably. The CMV in PMSMs drives is known to destroy winding insulations and generate common-mode current, which will cause severe electromagnetic interference (EMI) and undesired damage to motor bearings [14], [15]. To decrease the effects of CMV and improve system reliability, a lot of works have been reported to suppress the CMV of voltage source inverters (VSIs).

In the MPC methods for multilevel and multiphase VSIs, the virtual vectors constructed by the vectors with small CMV are usually defined as the candidates to reduce the CMV [16], [17]. Besides, additional CMV items are included in the cost function to penalize unexpected vectors with large CMV in multiphase VSIs [18], [19]. In the system consisting of a three-phase two-level inverter and PMSM, the zero vectors with large CMV are usually discarded to achieve CMV suppression. In [20], three adjacent nonzero vectors and one nonadjacent vector are utilized to evaluate the cost function during each sampling interval. However, the CMV reduction causes the increase of current distortion for the deprecation of zero vectors. In [21], the zero vectors are replaced by two opposite nonzero vectors to improve the

Manuscript received 4 July 2022; revised 22 October 2022; accepted 25 November 2022. Date of publication 7 December 2022; date of current version 14 February 2023. This work was supported in part by the National Natural Science Foundation of China under Grant 52022084 and in part by the Sichuan Youth Science and Technology Innovation Research Team Project under Grant 22CXTD0055. Recommended for publication by Associate Editor A. M. Trzynadlowski. *(Corresponding authors: Wensheng Song and Chenwei Ma.)*

The authors are with the School of Electrical Engineering, Southwest Jiaotong University, Chengdu 610031, China (e-mail: lijiayao_2021@163.com; songwengsheng@163.com; yuehao6866@163.com; sunnadq@my.swjtu.edu.cn; chenwei.ma@ugent.be; frswjtu@163.com).

Color versions of one or more figures in this article are available at https://doi.org/10.1109/TPEL.2022.3227436.

Digital Object Identifier 10.1109/TPEL.2022.3227436

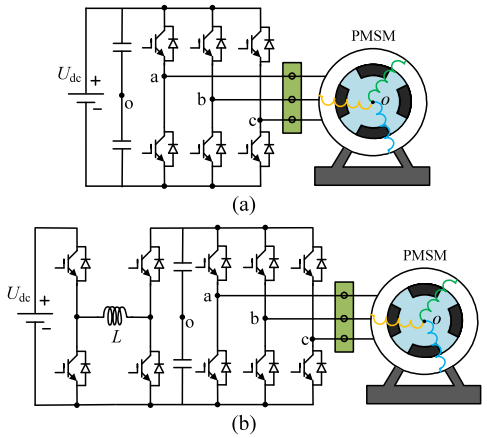

Fig. 1. Circuit topology of PMSM dive system. (a) Classic topology of three-phase VSI with PMSM. (b) Cascade topology formed by buck-boost converter and VSI with PMSM.

control accuracy. Furthermore, the vectors preselection strategy based on the current sector is proposed to eliminate CMV spikes caused by the dead-time effect. Nevertheless, the steady-state performance is still not satisfactory. To improve the steady-state performance further, a reduced-common-mode-voltage MPC (RCMV-MPC) is proposed in [22]. By adopting two nonzero vectors in each sampling interval, the synthesized vectors are closer to the reference vector. Thereby, the control precision is improved effectively. However, more opposite and nonadjacent vectors are used in the low-speed region, which increases the switching frequency and generates additional heat loss [22]. According to the above analysis, these CMV reduction schemes inevitably deteriorate the steady-state performance and increase the switching frequency.

Nowadays, PMSMs have achieved a lot of applications and development in the field of electric vehicles (EVs). With regard to the propulsion system in EVs, the following two basic configurations are used: the battery is connected to the dc input of VSI directly and a boost converter is placed between the battery and VSI. As shown in Fig. 1(a), the battery with constant voltage is connected directly to the dc-bus of the VSI in the classic topology of motor drives. Thanks to its single-stage conversion, the architecture in Fig. 1(a) is cheap, easy to manufacture and requires simple control, thereby this classic topology is widely used in EVs over the past decades [23]. At present, the drive system with higher supply voltage has become more popular due to its superior efficiency [24], [25]. Employing a boost converter followed by a dc–ac stage enables to enhance the dc-bus voltage of VSI, which can reduce the cost and size of the battery, and allow extensions of the speed range without field weakening [28]. In [26], [27], the applications of bidirectional buck-boost converter in EVs are further studied for its wider output voltage range, the cascade topology is shown in Fig. 1(b). By adopting the cascaded topology shown in Fig. 1(b), the dc-bus voltage can be adjusted by the dc–dc converter to adapt to more conditions. In this article, the possibilities to reduce CMV and current harmonics by using the topology shown in Fig. 1(b) are explored.

TABLE I
EIGHT VOLTAGE VECTORS AND THEIR CMV

vectors	$S_a\,S_b\,S_c$	CMV	vectors	$S_a\,S_b\,S_c$	CMV
$\boldsymbol{u}_0$	000	$-U_{dc}/2$	$\boldsymbol{u}_4$	011	$U_{dc}/6$
$\boldsymbol{u}_1$	100	$-U_{dc}/6$	$\boldsymbol{u}_5$	001	$-U_{dc}/6$
$\boldsymbol{u}_2$	110	$U_{dc}/6$	$\boldsymbol{u}_6$	101	$U_{dc}/6$
$\boldsymbol{u}_3$	010	$-U_{dc}/6$	$\boldsymbol{u}_7$	111	$U_{dc}/2$

To suppress the CMV, improve the control accuracy and reduce the switching frequency, an improved MPC method for PMSM drives with variable dc-bus voltage is proposed in this article. First, the virtual vectors with lower CMV and switching frequency are defined, the optimal virtual vector is selected and its duty cycle is calculated. Then, the limitation of the fixed dc-bus voltage is analyzed. Furthermore, the effects of the dc-bus voltage on current distortion are investigated, and the optimal reference dc-bus voltage is determined to minimize the current harmonics. Finally, the dc–dc converter is adopted to track the reference voltage. The main contributions of this article are summarized as follows.

1) By defining the virtual vectors with low CMV and switching frequency, the proposed method can reduce the CMV from $\pm U_{dc}/2$ to $\pm U_{dc}/6$ compared with DB-MPC in [12], and lower the switching frequency effectively compared with RCMV-MPC in [22].
2) By presenting the missing distribution of defined virtual vectors, the poor control accuracy at low speeds with fixed dc-bus voltage is illustrated. To overcome this limitation, the variability of dc-bus voltage is utilized fully in the proposed method to adjust the coverage of virtual vectors, thereby the control precision is improved significantly.
3) By establishing the model of peak-to-peak values of stator flux error, the effect of the dc-bus voltage on current distortion is analyzed in detail, and the optimal reference dc-bus voltage is determined to minimize the current distortion. Thereby, the steady-state performance is improved significantly compared with RCMV-MPC, and similar excellent compared with DB-MPC.

The rest of this article is structured as follows. Section II illustrates the model of the PMSM and conventional RCMV-MPC. The proposed method is described in Section III. Experimental results and conclusion are presented in Sections IV and V.

II. SYSTEM MODELING AND CONVENTIONAL RCMV-MPC

A. System Mathematical Model

The CMV in three-phase VSI can be expressed as [21]

$$u_{CM} = \frac{U_{dc}}{3}(S_a + S_b + S_c) - \frac{U_{dc}}{2} \tag{1}$$

where U_{dc} denotes the dc-bus voltage of VSI; S_a, S_b, and S_c represent the switching signals of three bridge arms. There are eight voltage vectors in three-phase VSI, and the CMV values of all vectors are given in Table I.

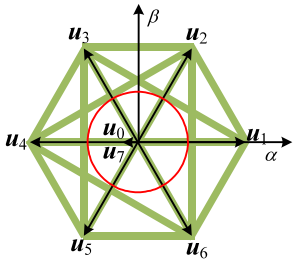

Fig. 2. Virtual vectors distribution in RCMV-MPC.

The mathematical model of PMSM in the *dq*- frame can be expressed as [6]

$$\begin{cases} \frac{di_d}{dt} = \frac{1}{L_d}(-Ri_d + u_d + L_q\omega_e i_q) \\ \frac{di_q}{dt} = \frac{1}{L_q}(-Ri_q + u_q - L_d\omega_e i_d - \omega_e\psi_f) \end{cases} \tag{2}$$

$$T_e = \frac{3}{2}n_p i_q[\psi_f + (L_d - L_q)i_d] \tag{3}$$

where u_d, u_q, and i_d, i_q represent *dq*-axis output voltages and currents; ω_e denotes rotor electrical angular velocity; ψ_f is permanent magnet flux linkage; L_d, L_q, and R represent the *dq*-axis stator inductances and winding resistance respectively; T_e is electromagnetic torque and n_p denotes the number of poles pairs.

The forward Euler method is utilized to discretize (2), then the current prediction model can be expressed as

$$\begin{cases} i_d^{k+1} = i_d^k + \frac{T_s}{L_d}(u_d^k - Ri_d^k + \omega_e L_q i_q^k) \\ i_q^{k+1} = i_q^k + \frac{T_s}{L_q}(u_q^k - Ri_q^k - \omega_e L_d i_d^k - \omega_e\psi_f) \end{cases} \tag{4}$$

where T_s is the sampling interval, the superscripts k and $k+1$ represent kth and $(k+1)$th sampling instants.

B. Analysis of Conventional RCMV-MPC

To suppress the CMV amplitude, an RCMV-MPC method is reported in [22]. The specific steps are as follows: First, the initial vector is obtained from six nonzero vectors by cost function minimization. Second, six nonzero vectors are selected as second candidate vectors, and the duty cycles of all virtual vectors composed of initial vector and second candidate vectors are calculated respectively. Finally, the virtual vector that minimizes the cost function is selected as the best virtual vector to generate switching pulses.

Fig. 2 presents the distribution of virtual vectors consisting of two non-zero vectors in RCMV-MPC. As shown in Fig. 2, the endpoints of the virtual vectors are distributed on the connecting line of every two nonzero vectors, that is, the green shaded area. Obviously, the distribution of virtual vectors is discontinuous, which may result in the loss of control accuracy. In addition, the candidate virtual vectors within the red circle are all composed of vectors in opposite directions, the higher switching frequency will be inevitable. Therefore, RCMV-MPC has the disadvantages of insufficient steady-state control accuracy and higher switching frequency at low speeds.

TABLE II
SWITCHING PULSE SEQUENCES OF SIX VIRTUAL VOLTAGE VECTORS

Initial vector	Optimal virtual vector	Pulse sequence of $\boldsymbol{u}_{vi}$
$\boldsymbol{u}_1$	$\boldsymbol{u}_{v1}$	$\boldsymbol{u}_6$—$\boldsymbol{u}_1$—$\boldsymbol{u}_2$—$\boldsymbol{u}_1$—$\boldsymbol{u}_6$
$\boldsymbol{u}_2$	$\boldsymbol{u}_{v2}$	$\boldsymbol{u}_1$—$\boldsymbol{u}_2$—$\boldsymbol{u}_3$—$\boldsymbol{u}_2$—$\boldsymbol{u}_1$
$\boldsymbol{u}_3$	$\boldsymbol{u}_{v3}$	$\boldsymbol{u}_2$—$\boldsymbol{u}_3$—$\boldsymbol{u}_4$—$\boldsymbol{u}_3$—$\boldsymbol{u}_2$
$\boldsymbol{u}_4$	$\boldsymbol{u}_{v4}$	$\boldsymbol{u}_3$—$\boldsymbol{u}_4$—$\boldsymbol{u}_5$—$\boldsymbol{u}_4$—$\boldsymbol{u}_3$
$\boldsymbol{u}_5$	$\boldsymbol{u}_{v5}$	$\boldsymbol{u}_4$—$\boldsymbol{u}_5$—$\boldsymbol{u}_6$—$\boldsymbol{u}_5$—$\boldsymbol{u}_4$
$\boldsymbol{u}_6$	$\boldsymbol{u}_{v6}$	$\boldsymbol{u}_5$—$\boldsymbol{u}_6$—$\boldsymbol{u}_1$—$\boldsymbol{u}_6$—$\boldsymbol{u}_5$

III. PROPOSED METHOD

Aiming at the aforementioned issues of RCMV-MPC, an improved MPC method with variable dc-bus voltage is proposed in this article. The principle and implementation of the proposed scheme are illustrated in this section.

A. Virtual Vector Selection and Duty Cycle Determination

To compensate for the one-step delay in MPC, the current values at $(k+1)$th sampling instant in (4) are usually regarded as the initial values for the next prediction. Then, the current values at $(k+2)$th sampling instant can be expressed as

$$\begin{cases} i_d^{k+2} = i_d^{k+1} + \frac{T_s}{L_d}[u_d^{k+1} - Ri_d^{k+1} + \omega_e L_q i_q^{k+1}] \\ i_q^{k+2} = i_q^{k+1} + \frac{T_s}{L_q}[u_q^{k+1} - Ri_q^{k+1} - \omega_e L_d i_d^{k+1} - \omega_e\psi_f] \end{cases} \tag{5}$$

where superscripts $k+2$ represents the $(k+2)$th sampling instant; ${u_d}^{k+1}$ and ${u_q}^{k+1}$ denote the *dq*- axis components of nonzero vectors $\boldsymbol{u}_i$ (i = 1–6). Furthermore, the cost function is

$$G = (i_d^* - i_d^{k+2})^2 + (i_q^* - i_q^{k+2})^2 \tag{6}$$

where ${i_d}^*$ and ${i_q}^*$ denote the *dq*- axis components of reference current values. The initial vector $\boldsymbol{u}_{opt}$ can be selected by the cost function minimization.

As given in Table I, zero vectors $\boldsymbol{u}_0$ and $\boldsymbol{u}_7$ have the largest CMV, -U_{dc}/2 and U_{dc}/2, respectively. To suppress the CMV, the zero vectors are discarded in this article. All the virtual vectors designed in the proposed method are named $\boldsymbol{u}_{v1}$–$\boldsymbol{u}_{v6}$, which are composed of three adjacent nonzero vectors. When the $\boldsymbol{u}_i$ is selected as the initial vector, the $\boldsymbol{u}_{vi}$ (i = 1–6) will be chosen as the optimal virtual vector. The pulse sequences of all virtual vectors are given in Table II.

As given in Table II, the optimal virtual vector $\boldsymbol{u}_{vi}$ is composed of $\boldsymbol{u}_i$ and two adjacent vectors $\boldsymbol{u}_x$ and $\boldsymbol{u}_y$. When the $\boldsymbol{u}_{vi}$ applied, the predicted current values at $(k+2)$th sampling instant can be obtained as

$$\begin{cases} i_d^{k+2} = i_d^{k+1} + s_{di}t_i + s_{dx}t_x + s_{dy}t_y \\ i_q^{k+2} = i_q^{k+1} + s_{di}t_i + s_{qx}t_x + s_{qy}t_y \\ T_s = t_i + t_x + t_y \end{cases} \tag{7}$$

where t_i, t_x, and t_y are the action times of $\boldsymbol{u}_i$, $\boldsymbol{u}_x$ and $\boldsymbol{u}_y$; s_{di}, s_{dx}, s_{dy} and s_{qi}, s_{qx}, s_{qy} are the *dq*- axis current slopes of $\boldsymbol{u}_i$, $\boldsymbol{u}_x$, and $\boldsymbol{u}_y$, their values can be obtained according to (2). Assuming the predicted currents shown in (7) are equal to the ${i_d}^*$ and ${i_q}^*$, then the durations of $\boldsymbol{u}_i$, $\boldsymbol{u}_x$, and $\boldsymbol{u}_y$ can be obtained.

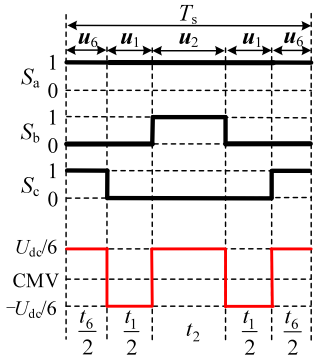

Fig. 3. Switching pulses and CMV of $\boldsymbol{u}_{v1}$.

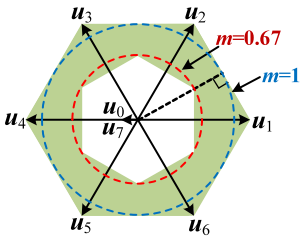

Fig. 4. Distribution of designed virtual vectors with fixed dc-bus voltage.

Taking $\boldsymbol{u}_{v1}$ as an example, its switching pulses and CMV are shown in Fig. 3, where t_6, t_1, and t_2 are the durations of $\boldsymbol{u}_6$, $\boldsymbol{u}_1$, and $\boldsymbol{u}_2$, respectively. In Fig. 3, the CMV is limited $-U_{\rm dc}/6$ to $U_{\rm dc}/6$, and only two-phase arms turn ON and turn OFF during one sampling interval. Therefore, the defined virtual vectors have a lower CMV and switching frequency.

B. Limitations of Fixed DC-Bus Voltage

The derivative of the currents in steady-state can be ignored in (2), thereby the dq- axis components of reference voltage ${u_d}^*$ and ${u_q}^*$ can be obtained as

$$\begin{cases} u_d^* = Ri_d^* - \omega_e L_q i_q^* \\ u_q^* = Ri_q^* + \omega_e L_d i_d^* + \omega_e \psi_f \end{cases}. \tag{8}$$

Then, the modulation index of the inverter is [28]

$$m = \frac{\sqrt{3}\,|\boldsymbol{u}^*|}{U_{\rm dc}} \tag{9}$$

where $|\boldsymbol{u}^*|$ is the magnitude of reference vector $\boldsymbol{u}^*$, its value is

$$|\boldsymbol{u}^*| = \sqrt{{u_d^*}^2 + {u_q^*}^2}. \tag{10}$$

As shown in Fig. 1(a), the dc-bus voltage in the classic topology is constant. Fig. 4 presents the distribution of designed virtual vectors with fixed dc voltage. In Fig. 4, the modulation index at the blue circle and red circle are 1 and 0.67, respectively [28]. The green area is the coverage of virtual vectors and all virtual vectors in green area are continuous. However, the control accuracy may be not satisfactory when $m < 0.67$ because the virtual vectors are discrete or even missing within the red circle.

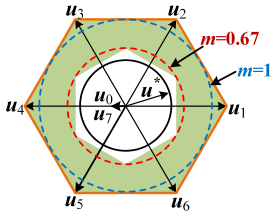

Fig. 5. Diagrams of hexagon and circles.

Therefore, the designed virtual vectors are not applicable under the fixed dc-bus voltage.

In addition, the freedom of dc-bus voltage is not utilized fully in Fig. 1(a). For example, the length of $\boldsymbol{u}^*$ will be short and a higher dc voltage is not necessary when the motor is running at low speed. Similarly, the length of $\boldsymbol{u}^*$ is so long that the supply voltage is not enough when the motor is running at high speed. By adopting the cascaded structure shown in Fig. 1(b), the dc-bus voltage can be adjusted to meet the requirements of more operating conditions, such as running at higher speed conditions without field weakening. The main purpose of this article is to use the adjustability of dc-bus voltage to reduce CMV and current distortion simultaneously.

C. Optimal Reference DC-Bus Voltage Calculation

As shown in Fig. 5, the endpoints of $\boldsymbol{u}_i$ ($i = 1$–6) constitute an orange hexagon. Since the length of $\boldsymbol{u}_i$ is $2U_{\rm dc}/3$, the hexagon will shrink and expand with the change of dc-bus voltage. Assuming $\boldsymbol{u}^*$ is constant, the endpoint of $\boldsymbol{u}^*$ will form a black circle as the motor rotates. Change the hexagon by adjusting the dc-bus voltage, so that the black circle will fall in the green area. Consequently, the error between virtual vectors and the reference vector will be effectively reduced. In other words, the control precision can be improved when $0.67 \le m \le 1$.

According to (9), the reference dc-bus voltage of VSI can be obtained as

$$U_{\rm dcref} = \frac{\sqrt{3}\,|\boldsymbol{u}^*|}{m}. \tag{11}$$

However, the optional range of $U_{\rm dcref}$ is relatively large when $0.67 \le m \le 1$ according to (11). The durations of applied voltages are different with diverse $U_{\rm dcref}$, which will lead to different current distortion. Therefore, the effect of dc-bus voltage on current distortion needs to be investigated, and the optimal $U_{\rm dcref}$ should be determined to minimize the current harmonics.

As given in Table II, the optimal virtual vector is applied in each sampling interval. During each sampling interval, the voltage errors must be generated when the instantaneous voltages are different from the constant reference voltage, which will cause distortion of the line current. Take the virtual vector $\boldsymbol{u}_{v2}$ as an example, the instantaneous error voltages of $\boldsymbol{u}_{v2}$ can be expressed as

$$\begin{cases} \boldsymbol{u}_{\rm err1} = \boldsymbol{u}_1 - \boldsymbol{u}^* \\ \boldsymbol{u}_{\rm err2} = \boldsymbol{u}_2 - \boldsymbol{u}^* \\ \boldsymbol{u}_{\rm err3} = \boldsymbol{u}_3 - \boldsymbol{u}^* \end{cases} \tag{12}$$

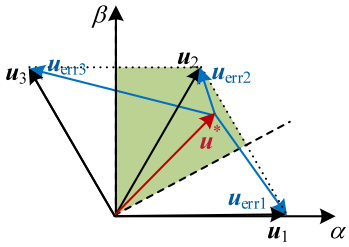

Fig. 6. Distribution of error voltage vectors.

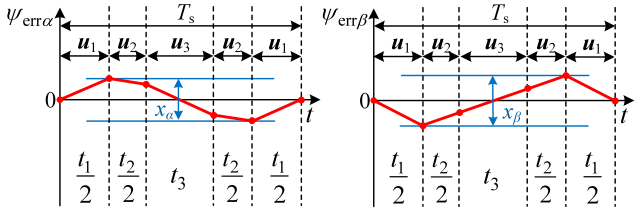

Fig. 7. Variation of stator flux error of $\boldsymbol{u}_{v2}$ when $u_{\mathrm{err}2\alpha} \leq 0$. (a) α- axis. (b) β- axis.

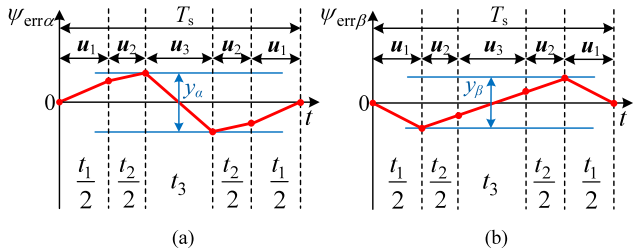

Fig. 8. Variation of stator flux error of $\boldsymbol{u}_{v2}$ when $u_{\mathrm{err}2\alpha} \leq 0$. (a) α- axis. (b) β- axis.

where $\boldsymbol{u}_{\mathrm{err}1}$, $\boldsymbol{u}_{\mathrm{err}2}$, and $\boldsymbol{u}_{\mathrm{err}3}$ represent the error voltage vectors corresponding to $\boldsymbol{u}_1$, $\boldsymbol{u}_2$, and $\boldsymbol{u}_3$. Fig. 6 presents the distribution of the error voltage vectors. According to Table II, the initial vector is $\boldsymbol{u}_2$ and the $\boldsymbol{u}^*$ is located in the green area when the $\boldsymbol{u}_{v2}$ is taken as an example [29], as shown in Fig. 6.

Since the length of $\boldsymbol{u}_i\,(i=1\text{–}6)$ is $2U_{\mathrm{dc}}/3$, the $\alpha\beta$- components of the error voltage vectors can be expressed as (13) according to Fig. 6, where u_α^* and $u_\beta{}^*$ are the $\alpha\beta$-axis components of $\boldsymbol{u}^*$.

$$\begin{cases} u_{\mathrm{err}1\alpha} = \frac{2U_{\mathrm{dc}}}{3} - |u_\alpha^*| \\ u_{\mathrm{err}1\beta} = -\left|u_\beta^*\right| \\ u_{\mathrm{err}2\alpha} = \frac{U_{\mathrm{dc}}}{3} - |u_\alpha^*| \\ u_{\mathrm{err}2\beta} = \frac{\sqrt{3}U_{\mathrm{dc}}}{3} - \left|u_\beta^*\right| \\ u_{\mathrm{err}3\alpha} = -\frac{U_{\mathrm{dc}}}{3} - |u_\alpha^*| \\ u_{\mathrm{err}3\beta} = \frac{\sqrt{3}U_{\mathrm{dc}}}{3} - \left|u_\beta^*\right| \end{cases}. \tag{13}$$

According to Fig. 6 and (13), it can be determined whether the other $\alpha\beta$-components of $\boldsymbol{u}_{\mathrm{err}1}$, $\boldsymbol{u}_{\mathrm{err}2}$, and $\boldsymbol{u}_{\mathrm{err}3}$ are positive or negative, except for $u_{\mathrm{err}2\alpha}$. The positive and negative of $\alpha\beta$-components of $\boldsymbol{u}_{\mathrm{err}1}$, $\boldsymbol{u}_{\mathrm{err}2}$ and $\boldsymbol{u}_{\mathrm{err}3}$ are given in Table III.

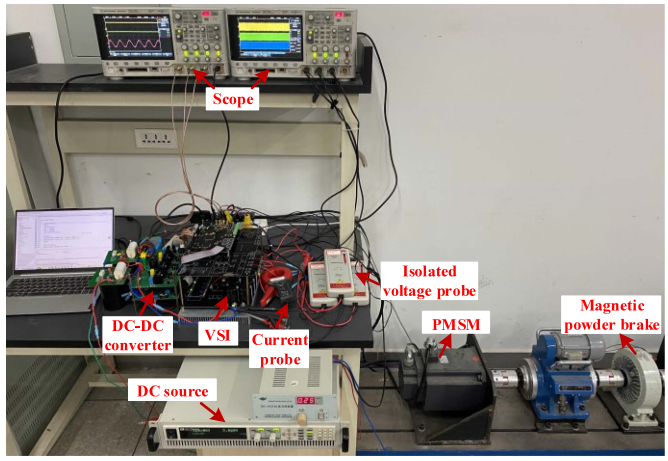

Fig. 9. Photo of experimental platform.

TABLE III
POSITIVE AND NEGATIVE OF COMPONENTS OF ERROR VOLTAGES

α-axis error voltages	Values	β-axis error voltages	Values
$u_{\mathrm{err}1\alpha}$	positive	$u_{\mathrm{err}1\beta}$	negative
$u_{\mathrm{err}2\alpha}$	positive or negative	$u_{\mathrm{err}2\beta}$	positive
$u_{\mathrm{err}3\alpha}$	negative	$u_{\mathrm{err}3\beta}$	positive

The time integral of the error voltage vector is termed as stator flux error vector [30]. When it satisfies $u_{\mathrm{err}2\alpha} \leq 0$, the variation of stator flux error of $\boldsymbol{u}_{v2}$ within a sampling period is shown in Fig. 7, where $\psi_{\mathrm{err}\alpha}$ and $\psi_{\mathrm{err}\beta}$ denote the $\alpha\beta$- axis components of stator flux error vector, x_α and x_β are the peak-to-peak values of $\psi_{\mathrm{err}\alpha}$ and $\psi_{\mathrm{err}\beta}$.

The t_1, t_2, and t_3 shown in Fig. 7 are the durations of $\boldsymbol{u}_1$, $\boldsymbol{u}_2$, and $\boldsymbol{u}_3$. By establishing the volt-second balance, the t_1, t_2 and t_3 can be expressed as

$$\begin{cases} t_1 = \frac{U_{\mathrm{dc}} - \sqrt{3}u_\beta^*}{U_{\mathrm{dc}}} T_s \\ t_2 = \frac{-U_{\mathrm{dc}} + 1.5u_\alpha^* + 1.5\sqrt{3}u_\beta^*}{U_{\mathrm{dc}}} T_s \\ t_3 = \frac{U_{\mathrm{dc}} - 1.5u_\alpha^* - 0.5\sqrt{3}u_\beta^*}{U_{\mathrm{dc}}} T_s \end{cases}. \tag{14}$$

It can be known from Fig. 7 that the vector sequence and waveforms of $\psi_{\mathrm{err}\alpha}$ and $\psi_{\mathrm{err}\beta}$ are symmetrical. Therefore, the α- axis stator flux error of $\boldsymbol{u}_{v2}$ within a half sampling period can be expressed as

$$\psi_{\mathrm{err}\alpha} = \begin{cases} u_{\mathrm{err}1\alpha} t & 0 \leq t \leq 0.5t_1 \\ 0.5u_{\mathrm{err}1\alpha}t_1 + u_{\mathrm{err}2\alpha}t & 0 \leq t \leq 0.5t_2 \\ 0.5u_{\mathrm{err}1\alpha}t_1 + 0.5u_{\mathrm{err}2\alpha}t_2 + u_{\mathrm{err}3\alpha}t & 0 \leq t \leq 0.5t_3 \end{cases}. \tag{15}$$

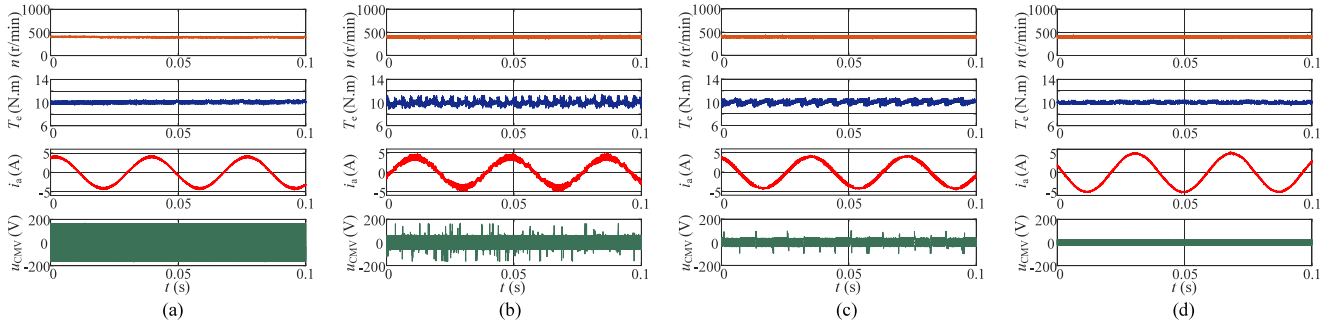

Fig. 10. Steady-state experimental waveforms of four control methods at 400 r/min (from top to bottom, waveforms are rotor speed, electromagnetic torque, a-phase current and CMV). (a) Deadbeat MPC. (b) RCMV-MPC. (c) Proposed method with $m = 0.67$. (d) Proposed method with $m = 1$.

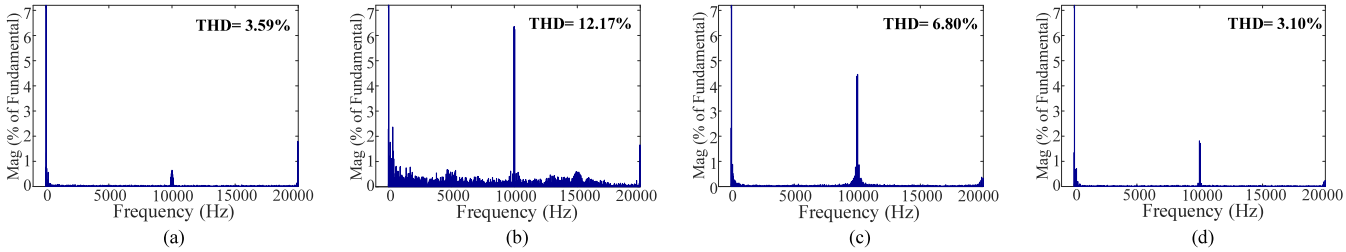

Fig. 11. THD values of i_a in four control methods at 400 r/min. (a) Deadbeat MPC. (b) Reduced-common-mode-voltage MPC. (c) Proposed method with $m = 0.67$. (d) Proposed method with $m = 1$.

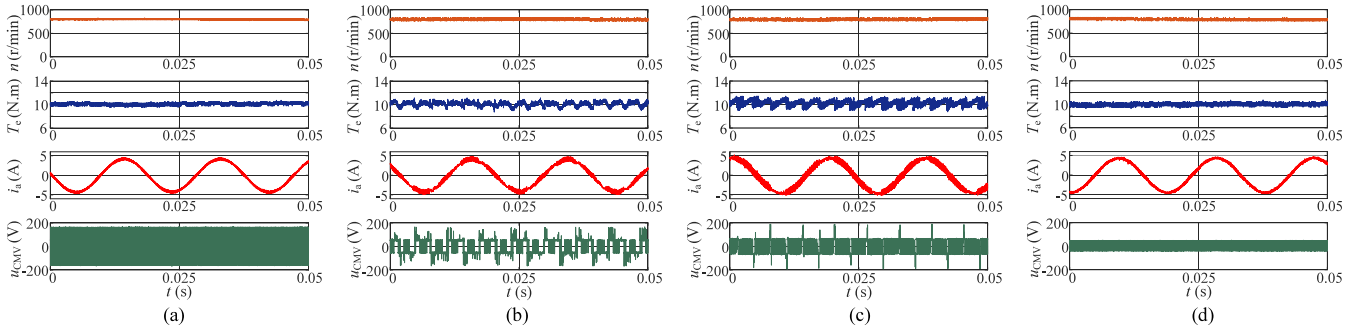

Fig. 12. Steady-state experimental waveforms of four control methods at 800 r/min (from top to bottom, waveforms are rotor speed, electromagnetic torque, a-phase current and CMV). (a) Deadbeat MPC. (b) Reduced-common-mode-voltage MPC. (c) Proposed method with $m = 0.67$. (d) Proposed method with $m = 1$.

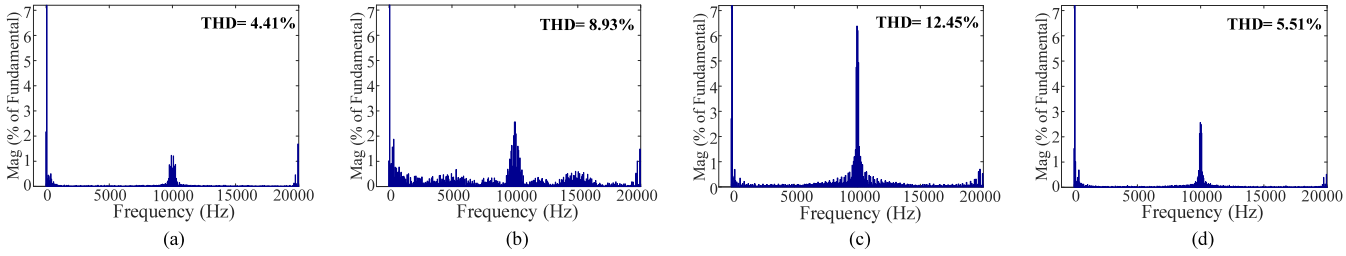

Fig. 13. THD values of i_a in four control methods at 800 r/min. (a) Deadbeat MPC. (b) Reduced-common-mode-voltage MPC. (c) Proposed method with $m = 0.67$. (d) Proposed method with $m = 1$.

Similarly, the β- axis stator flux error of $\boldsymbol{u}_{v2}$ within a half sampling period can be expressed as

$$\psi_{\mathrm{err}\beta} = \begin{cases} u_{\mathrm{err}1\beta}t & 0 \le t \le 0.5t_1 \\ 0.5u_{\mathrm{err}1\beta}t_1 + u_{\mathrm{err}2\beta}t & 0 \le t \le 0.5t_2 \\ 0.5u_{\mathrm{err}1\beta}t_1 + 0.5u_{\mathrm{err}2\beta}t_2 + u_{\mathrm{err}3\beta}t & 0 \le t \le 0.5t_3 \end{cases}. \tag{16}$$

In this article, the peak-to-peak values of $\psi_{\mathrm{err}\alpha}$ and $\psi_{\mathrm{err}\beta}$ are utilized to evaluate current distortion. To obtain minimum current distortion, the peak-to-peak values should be minimum. As shown in Fig. 7, the peak-to-peak values of $\psi_{\mathrm{err}\alpha}$ and $\psi_{\mathrm{err}\beta}$ when $u_{\mathrm{err}2\alpha} \le 0$ can be expressed as

$$\begin{cases} x_\alpha = u_{\mathrm{err}1\alpha}t_1 \\ x_\beta = u_{\mathrm{err}2\beta}\left(t_2 + t_3\right) \end{cases}. \tag{17}$$

To analyze the relationship between peak-to-peak values x_α, x_β and dc-bus voltage, the derivative of (17) is obtained as

$$\begin{cases} \frac{\partial x_\alpha}{\partial U_{\mathrm{dc}}} = \frac{\sqrt{3}\left(\frac{2U_{\mathrm{dc}}}{3} - |u_\alpha^*|\right)\left(\frac{\sqrt{3}U_{\mathrm{dc}}}{3} - |u_\beta^*|\right)}{U_{\mathrm{dc}}^2} \ge 0 \\ \frac{\partial x_\beta}{\partial U_{\mathrm{dc}}} = \frac{\sqrt{3}|u_\beta^*|^2 T_s}{U_{\mathrm{dc}}^2} \ge 0 \end{cases}. \tag{18}$$

Therefore, x_α and x_β are the increasing functions of U_{dc}, which means that if U_{dc} is smaller, the values of x_α and x_β are smaller.

When it satisfies $u_{\mathrm{err}2\alpha} \le 0$, the variation of stator flux error of $\boldsymbol{u}_{v2}$ within a sampling period is shown in Fig. 8, where y_α and y_β are the peak-to-peak values of $\psi_{\mathrm{err}\alpha}$ and $\psi_{\mathrm{err}\beta}$.

As shown in Fig 8, the peak-to-peak values of $\psi_{\mathrm{err}\alpha}$ and $\psi_{\mathrm{err}\beta}$ when $u_{\mathrm{err}2\alpha} \le 0$ can be expressed as

$$\begin{cases} y_\alpha = u_{\mathrm{err}1\alpha}t_1 + u_{\mathrm{err}2\alpha}t_2 \\ y_\beta = x_\beta \end{cases}. \tag{19}$$

To analyze the relationship between peak-to-peak values y_α, y_β and dc-bus voltage, the derivative of (19) is obtained as

$$\begin{cases} \frac{\partial y_\alpha}{\partial U_{\mathrm{dc}}} = \frac{\frac{U_{\mathrm{dc}}^2}{3} + \frac{\sqrt{3}}{2}|u_\alpha^*|\left|u_\beta^*\right| + \frac{3}{2}|u_\alpha^*|^2}{U_{\mathrm{dc}}^2} \ge 0 \\ \frac{\partial y_\beta}{\partial U_{\mathrm{dc}}} = \frac{\partial x_\beta}{\partial U_{\mathrm{dc}}} \ge 0 \end{cases}. \tag{20}$$

Therefore, y_α and y_β are also the increasing functions of U_{dc}, which means that if U_{dc} is smaller, the values of y_α and y_β are smaller as well. The above analysis shows that no matter whether $u_{\mathrm{err}2\alpha}$ is positive or negative, the peak-to-peak values of flux error and current distortion decrease with the decrease of U_{dc}. Similarly, the same conclusion can be obtained when the optimal virtual vector is a different one. To minimize the current distortion, the dc-bus voltage of VSI should be as small as possible. It can be known from (11) that if m is bigger when $0.67 \le m \le 1$, the reference dc-bus voltage U_{dcref} is smaller. To obtain the minimum possible U_{dc}, the value of m should be set to 1. Thereby, the optimal U_{dcref} is obtained as

$$U_{\mathrm{dcref}} = \sqrt{3}\left|\boldsymbol{u}^*\right|. \tag{21}$$

TABLE IV
PARAMETERS OF EXPERIMENTAL PLATFORM

Parameter	Symbol	Value
Rated speed	n	1500 r/min
d- axis inductance	L_d	6.24 mH
q- axis inductance	L_q	6.24 mH
Stator resistance	R	0.71 Ω
PM flux linkage	Ψ_{f}	0.421 Wb
Pole pairs	n_{p}	4

To avoid the torque oscillation caused by insufficient dc-bus voltage in dynamic conditions, the reference dc-bus voltage with compensation is further modified as

$$U_{\mathrm{dcref}} = \begin{cases} \sqrt{3}\left|\boldsymbol{u}^*\right| & n^* - n \le 50 \text{ r/min} \\ \frac{\sqrt{3}|\boldsymbol{u}^*|}{0.9} & n^* - n > 50 \text{ r/min} \end{cases} \tag{22}$$

where n^* and n are reference rotor speed and real speed, respectively. As shown in (22), it satisfies $m = 1$ when n^*-$n \le 50$ r/min and $m = 0.9$ when n^*-$n > 50$ r/min, which means U_{dcref} remains minimum in steady state and has a slight increase in the dynamic state.

Furthermore, the dc-bus voltage of inverter can be adjusted to track U_{dcref} by adopting dc–dc converters, which is widely used in the next-generation 800 V-level EVs. The control method of dc–dc converter is described in detail in [31], which will not be repeated in this article.

IV. EXPERIMENTAL RESULTS

Fig. 9 shows a scale-down experimental platform of three phase VSI with PMSM. In this platform, the control methods are programmed and implemented in TI DSP TMS320F28335.

The output voltage u_{ao}, u_{bo}, and u_{co} shown in Fig. 1 are measured by isolated voltage probes, and the CMV is obtained by [20]

$$u_{\mathrm{CMV}} = \frac{1}{3}\left(u_{\mathrm{ao}} + u_{\mathrm{bo}} + u_{\mathrm{co}}\right). \tag{23}$$

The parameters of PMSM are given in Table IV. In this Section, the DB-MPC in [12], RCMV-MPC in [22] are compared, as well as the proposed methods with different m values, where different values of m lead to different reference dc-bus voltage. The fix dc-bus voltage of VSI in DB-MPC and RCMV-MPC is 320 V, which ensures that the PMSM runs in the speed range of 0 to 1000 r/min. The dc input voltage of the buck-boost converter adopted in proposed method are 200 V, and the dc-bus voltage of the VSI is adjusted according to (22). The sampling frequencies of studied methods are all 10 kHz.

A. Steady-State Performance Comparison

To compare the steady-state performance of different control methods, Fig. 10 presents the rotor speed, torque, a-phase current and CMV waveforms, Fig. 11 shows the fast Fourier transform (FFT) analysis of a-phase current i_{a}, where the load torque and the speed are 10 N.m and 400 r/min, respectively.

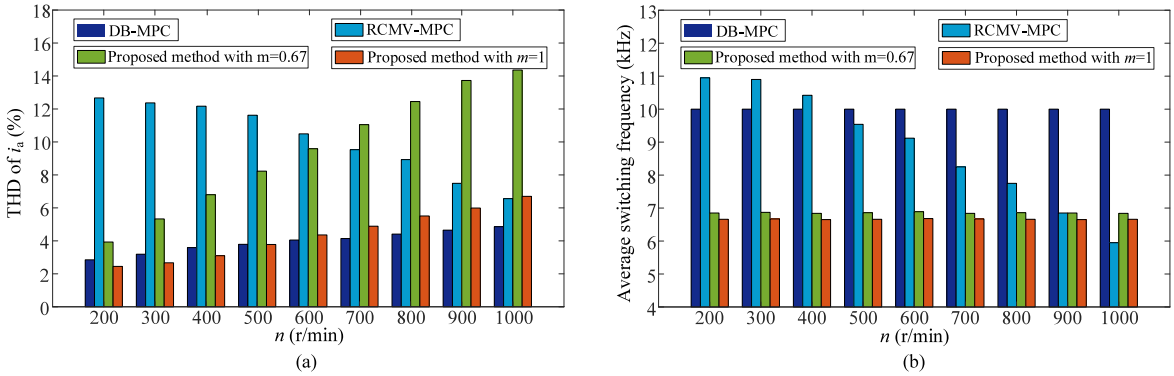

Fig. 14. Current THD and average switching frequency of four methods at different speeds. (a) THD values of i_a. (b) Average switching frequency.

As shown in Figs. 10 and 11, the DB-MPC has smaller torque ripple and current distortion than RCMV-MPC and the proposed method with $m = 0.67$, however, the CMV amplitude is $\pm U_{dc}/2$ due to the utilization of zero vectors. The RCMV-MPC reduced the CMV amplitude to $\pm U_{dc}/6$ effectively, although there are some CMV spikes, which is due to the effect of dead times in the real experimental setup [32], [32], and is not discussed in this article. Nevertheless, severe torque ripple and current distortion are inevitable in RCMV-MPC because the candidate vectors are discontinuous. On the contrary, the candidate vectors in the proposed method are continuous. Consequently, the steady-state performances are improved. Meanwhile, the CMV reduction is achieved simultaneously. As illustrated in Section III-C, the reference dc-bus voltages are different with diverse m, which will lead to different current distortion. As shown in Figs. 10 and 11, the proposed method with $m = 1$ has lower current distortion than the proposed method with $m = 0.67$, which verifies the correctness of the theoretical analysis in Section III-C. In addition, by taking full advantage of the variability of dc-bus voltage, the proposed method with $m = 1$ has similar excellent steady-state performance similar to DB-MPC.

Figs. 12 and 13 present the steady-state experimental waveforms and the FFT analysis of i_a, where the load torque and the speed are 10 N.m and 800 r/min, respectively. As shown in Figs. 12 and 13, the CMV reduction can be achieved both in RCMV-MPC and the proposed methods, yet the proposed method with $m = 1$ has the lower current harmonics and torque ripple than RCMV-MPC.

To compare the steady-state performances at different speeds, Fig. 14(a) and (b) show the current THD and average switching frequencies of four methods, where the load torque is 10 N.m. The average switching frequency is defined as

$$f_{sw} = \frac{1}{3T_w} \sum_{k=a}^{c} N_k \tag{24}$$

where T_w is the time window for counting the ON-OFF times of IGBTs, and T_w is set to 1 s in this test. N_k is the ON-OFF times of leg k (k = a, b, c).

As shown in Fig. 14(a), the current THD values of proposed method with $m = 1$ are closed to DB-MPC, and much lower than RCMV-MPC and proposed method with $m = 0.67$. As shown in Fig. 14(b), the average switching frequencies of proposed method with $m = 1$ are closed to proposed method with $m = 0.67$, and lower than DB-MPC and RCMV-MPC, especially in the low-speed conditions.

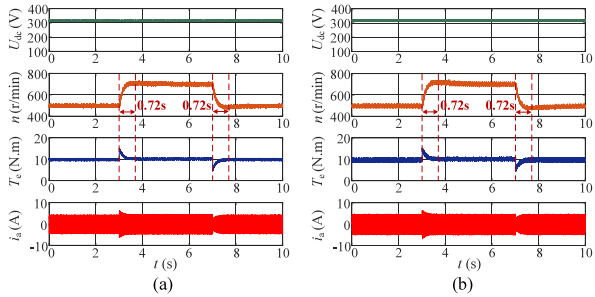

Fig. 15. Dynamic waveforms of two conventional methods when speed steps up and down (from top to bottom, waveforms are DC-bus voltage, rotor speed, electromagnetic torque, a-phase current). (a) Deadbeat MPC. (b) Reduced-common-mode-voltage MPC.

B. Dynamic Performance Comparison

As shown in Fig. 14, the current harmonics of the proposed method with $m = 1$ is lower than the proposed method with $m = 0.67$, and their average switching frequencies are similar. Therefore, the proposed method with $m = 1$ has better performance. To simplify the analysis, only the dynamic performances of DB-MPC, RCMV-MPC and the proposed method with $m = 1$ have been compared in this article. Fig. 15 shows the dynamic waveforms of DB-MPC and RCMV-MPC when the speed steps up from 500 to 700 r/min at 3 s and steps down from 700 to 500 r/min at 7 s, where the load torque is 10 N.m. Figs. 16 and 17 show the dynamic waveforms of the proposed method with $m = 1$. It should be noticed that the reference dc-bus voltage in Fig. 16 is obtained by (21) and without any additional compensation. On the contrary, the reference dc-bus voltage in Fig. 17 is obtained by (22) and with compensation.

As shown in Figs. 15–17, the dc-bus voltage of DB-MPC and RCMV-MPC are constant, while the dc-bus voltage of the proposed method with $m = 1$ varies with speed and torque. In

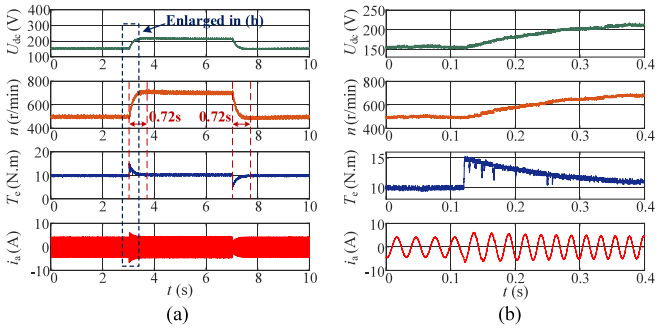

Fig. 16. Dynamic waveforms of the proposed method with $m = 1$ without compensation when speed steps up and down (from top to bottom, waveforms are DC-bus voltage, rotor speed, electromagnetic torque, a-phase current).

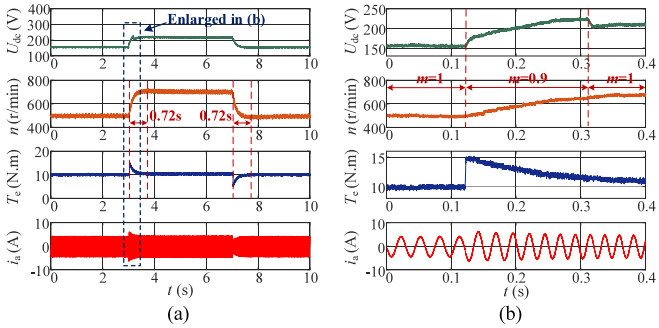

Fig. 17. Dynamic waveforms of the proposed method with $m = 1$ with compensation when speed steps up and down (from top to bottom, waveforms are DC-bus voltage, rotor speed, electromagnetic torque, and a-phase current).

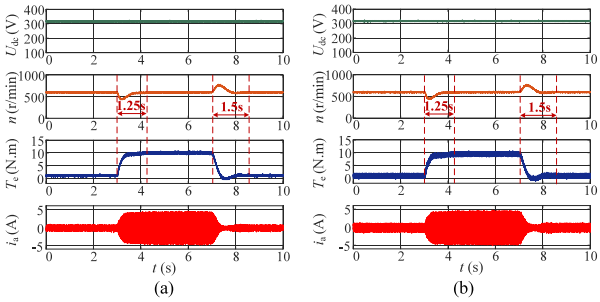

Fig. 18. Dynamic waveforms of two conventional methods when load torque steps up and down (from top to bottom, waveforms are DC-bus voltage, rotor speed, electromagnetic torque, a-phase current). (a) Deadbeat MPC. (b) Reduced-common-mode-voltage MPC.

addition, the settling times of the speed and torque corresponding to the studied methods are nearly the same. In Fig.16, a slight torque oscillation exists in the proposed method without compensation when the speed steps up. The reason for this problem is that the dc-bus voltage is not large enough when speed steps up. By adding a certain compensation, the dc-bus voltage has a slight increase when speed steps up and the torque oscillation is effectively eliminated, as shown in Fig. 17.

Figs. 18 and 19 show the dynamic waveforms of DB-MPC, RCMV-MPC and the proposed method with $m = 1$ with compensation, where the load torque steps up from 1 to 10 N.m at

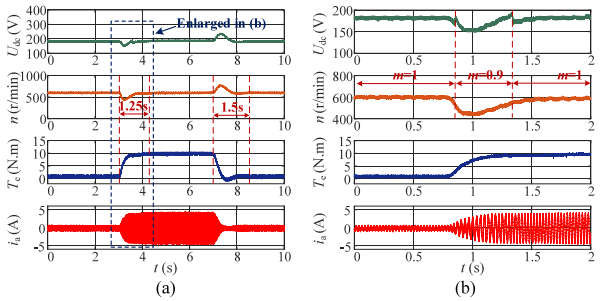

Fig. 19. Dynamic waveforms of the proposed method with $m = 1$ with compensation when load torque steps up and down (from top to bottom, waveforms are DC-bus voltage, rotor speed, electromagnetic torque, a-phase current).

TABLE V
COMPARISON BETWEEN PROPOSED METHOD AND CONVENTIONAL METHODS

Method	CMV Reduction	Steady-state Performance	Dynamic Performance	Switching Frequency
DB-MPC	No	good	fast	high
RCMV-MPC	Yes	worse	fast	high
Proposed method with m=0.67	Yes	worse	fast	low
Proposed method with m=1	Yes	good	fast	low

3 s and steps down from 10 to 1 N.m at 7 s. As shown in Figs. 18 and 19, the dc-bus voltage of DB-MPC and RCMV-MPC are constant, while the dc-bus voltage of the proposed method with $m = 1$ varies with speed and torque. In addition, the settling times of the speed and torque corresponding to the three methods are nearly the same, and no torque oscillation occurs in the proposed method with $m = 1$ with compensation when the load torque steps up and steps down.

C. Overall Comparison of Four Control Methods

Finally, in order to present a clear evaluation of the studied methods, a comprehensive comparison is given in Table IV. In Table V, DB-MPC has excellent steady-state performance, while the CMV reduction is not considered. The CMV reduction is achieved both in RCMV-MPC and the proposed method. However, the RCMV-MPC shows the worse steady-state performance and higher average switching frequency in low-speed region. By redefining the virtual vectors, the proposed method reduces the CMV and switching frequency effectively, where the different values of m correspond to different reference dc-bus voltages. By taking full advantage of the variability of dc-bus voltage, the proposed method with $m = 1$ has better steady-state performance than RCMV-MPC and the proposed method with $m = 0.67$, and similar excellent to DB-MPC.

V. CONCLUSION

This article proposes an improved MPC method for PMSM drives with variable dc-bus voltage, to suppress the CMV, improve the control accuracy and reduce the switching frequency. The virtual vectors with lower CMV and switching frequency

are designed. Then, the limitation of designed virtual vectors with fixed dc-bus voltage is investigated. On the basis of analyzing the effects of dc-bus voltage on current distortion, the optimal reference dc-bus voltage is calculated to minimize the current harmonics. Finally, the dc–dc converter is adopted to adjust the dc-bus voltage according to the reference voltage. An experimental comparison of the conventional methods and the proposed scheme is implemented. From the experimental analysis, the conclusions can be summarized as follows.

1) The proposed method can reduce the CMV to $\pm U_{\rm dc}/6$, which is lower than DB-MPC and equal to RCMV-MPC.
2) Compared with RCMV-MPC, the proposed method can significantly reduce the current distortion and switching frequency, especially in the low-speed conditions.
3) Compared with DB-MPC, the proposed method with $m = 1$ has the similar excellent steady-state performance.
4) The current harmonics of the proposed method decrease with the decrease of dc-bus voltage, and the optimal dc-bus reference voltage calculated by $m = 1$ can minimize the current harmonics.

REFERENCES

[1] X. Jiang et al., "An improved implicit model predictive current control with continuous control set for PMSM drives," *IEEE Trans. Transp. Electrific.*, vol. 8, no. 2, pp. 2444–2455, Jun. 2022.

[2] K. Zhang, M. Fan, Y. Yang, Z. Zhu, C. Garcia, and J. Rodriguez, "An improved adaptive selected harmonic elimination algorithm for current measurement error correction of PMSMs," *IEEE Trans. Power Electron.*, vol. 36, no. 11, pp. 13128–13138, Nov. 2021.

[3] Z. Zhang, Z. Li, M. P. Kazmierkowski, J. Rodríguez, and R. Kennel, "Robust predictive control of three-level NPC back-to-back power converter PMSG wind turbine systems with revised predictions," *IEEE Trans. Power Electron.*, vol. 33, no. 11, pp. 9588–9598, Nov. 2018.

[4] Z. Zhang, H. Fang, F. Gao, J. Rodríguez, and R. Kennel, "Multiple-vector model predictive power control for grid-tied wind turbine system with enhanced steady-state control performance," *IEEE Trans. Ind. Electron.*, vol. 64, no. 8, pp. 6287–6298, Aug. 2017.

[5] Y. Yang et al., "Low complexity finite-control-set MPC based on discrete space vector modulation for T-type three-phase three-level converters," *IEEE Trans. Power Electron.*, vol. 37, no. 1, pp. 392–403, Jan. 2022.

[6] J. Rodriguez et al., "Predictive current control of a voltage source inverter," *IEEE Trans. Ind. Electron.*, vol. 54, no. 1, pp. 495–503, Feb. 2007.

[7] M. Preindl and S. Bolognani, "Model predictive direct torque control with finite control set for PMSM drive systems, part 1: Maximum torque per ampere operation," *IEEE Trans. Ind. Inform.*, vol. 9, no. 4, pp. 1912–1921, Nov. 2013.

[8] S. G. Petkar and V. K. Thippiripati, "Enhanced predictive current control of PMSM drive with virtual voltage space vectors," *IEEE J. Emerg. Sel. Topics Power Electron.*, vol. 3, no. 3, pp. 834–844, Jul. 2022, doi: 10.1109/JESTIE.2021.3105316.

[9] M. R. Nikzad, B. Asaei, and S. O. Ahmadi, "Discrete duty-cycle-control method for direct torque control of induction motor drives with model predictive solution," *IEEE Trans. Power Electron.*, vol. 33, no. 3, pp. 2317–2329, Mar. 2018.

[10] Y. Zhang and H. Yang, "Two-vector-based model predictive torque control without weighting factors for induction motor drives," *IEEE Trans. Power Electron.*, vol. 31, no. 2, pp. 1381–1390, Feb. 2016.

[11] H. Chen, H. Kim, R. Erickson, and D. Maksimović, "Electrified automotive powertrain architecture using composite DC–DC converters," *IEEE Trans. Power Electron.*, vol. 32, no. 1, pp. 98–116, Jan. 2017.

[12] H.-T. Moon, H.-S. Kim, and M.-J. Youn, "A discrete-time predictive current control for PMSM," *IEEE Trans. Power Electron.*, vol. 18, no. 1, pp. 464–472, Jan. 2003.

[13] X. Zhang, B. Hou, and Y. Mei, "Deadbeat predictive current control of permanent-magnet synchronous motors with stator current and disturbance observer," *IEEE Trans. Power Electron.*, vol. 32, no. 5, pp. 3818–3834, May 2017.

[14] Z. Liu, Z. Zheng, S. D. Sudhoff, C. Gu, and Y. Li, "Reduction of common-mode voltage in multiphase two-level inverters using SPWM with phase-shifted carriers," *IEEE Trans. Power Electron.*, vol. 31, no. 9, pp. 6631–6645, Sep. 2016.

[15] R. Karampuri, S. Jain, and V. T. Somasekhar, "Common-mode current elimination PWM strategy along with current ripple reduction for open winding five-phase induction motor drive," *IEEE Trans. Power Electron.*, vol. 34, no. 7, pp. 6659–6668, Jul. 2019.

[16] B. Yu, W. Song, Y. Guo, J. Li, and M. S. R. Saeed, "Virtual voltage vector-based model predictive current control for five-phase VSIs with common-mode voltage reduction," *IEEE Trans. Transp. Electrific.*, vol. 7, no. 2, pp. 706–717, Jun. 2021.

[17] B. Yu, W. Song, J. Li, B. Li, and M. S. R. Saeed, "Improved finite control set model predictive current control for five-phase VSIs," *IEEE Trans. Power Electron.*, vol. 36, no. 6, pp. 7038–7048, Jun. 2021.

[18] M. J. Duran, J. A. Riveros, F. Barrero, H. Guzman, and J. Prieto, "Reduction of common-mode voltage in five-phase induction motor drives using predictive control techniques," *IEEE Trans. Ind. Appl.*, vol. 48, no. 6, pp. 2059–2067, Nov./Dec. 2012.

[19] R. Vargas, U. Ammann, J. Rodriguez, and J. Pontt, "Predictive strategy to control common-mode voltage in loads fed by matrix converters," *IEEE Trans. Ind. Electron.*, vol. 55, no. 12, pp. 4372–4380, Dec. 2008.

[20] L. Guo, X. Zhang, S. Yang, Z. Xie, and R. Cao, "A model predictive control-based common-mode voltage suppression strategy for voltage-source inverter," *IEEE Trans. Ind. Electron.*, vol. 63, no. 10, pp. 6115–6125, Oct. 2016.

[21] L. Guo, N. Jin, C. Gan, L. Xu, and Q. Wang, "An improved model predictive control strategy to reduce common-mode voltage for two-level voltage source inverters considering dead-time effects," *IEEE Trans. Ind. Electron.*, vol. 66, no. 5, pp. 3561–3572, May 2019.

[22] S. Kwak and S. Mun, "Model predictive control methods to reduce common-mode voltage for three-phase voltage source inverters," *IEEE Trans. Power Electron.*, vol. 30, no. 9, pp. 5019–5035, Sep. 2015.

[23] J. Reimers, L. Dorn-Gomba, C. Mak, and A. Emadi, "Automotive traction inverters: Current status and future trends," *IEEE Trans. Veh. Technol.*, vol. 68, no. 4, pp. 3337–3350, Apr. 2019.

[24] H. Chen, H. Kim, R. Erickson, and D. Maksimović, "Electrified automotive powertrain architecture using composite DC–DC converters," *IEEE Trans. Power Electron.*, vol. 32, no. 1, pp. 98–116, Jan. 2017.

[25] N. Zhao, N. Schofield, R. Yang, and R. Gu, "Investigation of DC-link voltage and temperature variations on EV traction system design," *IEEE Trans. Ind. Appl.*, vol. 53, no. 4, pp. 3707–3718, Jul./Aug. 2017.

[26] N. Su, D. Xu, M. Chen, and J. Tao, "Study of bi-directional buck-boost converter with different control methods," in *Proc. IEEE Veh. Power Propulsion Conf.*, 2008, pp. 1–5.

[27] K. Zhiguo, Z. Chunbo, Y. Shiyan, and C. Shukang, "Study of bidirectional DC-DC converter for power management in electric bus with super capacitors," in *Proc. IEEE Veh. Power Propulsion Conf.*, 2006, pp. 1–5.

[28] X. Zhang, B. Wang, Y. Yu, J. Zhang, and D. Xu, "Minimum-nonlinear-voltage method for torque ripple suppression in induction motor overmodulation and field-weakening control," *IEEE Trans. Ind. Electron.*, vol. 69, no. 5, pp. 4495–4509, May 2022.

[29] Y. Zhang, D. Xu, J. Liu, S. Gao, and W. Xu, "Performance improvement of model-predictive current control of permanent magnet synchronous motor drives," *IEEE Trans. Ind. Appl.*, vol. vol. 53, no.no. 4, pp. 3683–3695, Jul./Aug. 2017.

[30] S. Das, G. Narayanan, and M. Pandey, "Space-vector-based hybrid pulse width modulation techniques for a three-level inverter," *IEEE Trans. Power Electron.*, vol. 29, no. 9, pp. 4580–4591, Sep. 2014.

[31] C.-H. Tsai, Y.-S. Tsai, and H.-C. Liu, "A stable mode-transition technique for a digitally controlled non-inverting buck–boost DC–DC converter," *IEEE Trans. Ind. Electron.*, vol. 62, no. 1, pp. 475–483, Jan. 2015.

[32] Q.-H. Tran and H.-H. Lee, "An advanced modulation strategy for three to-five-phase indirect matrix converters to reduce common-mode voltage with enhanced output performance," *IEEE Trans. Ind. Electron.*, vol. 65, no. 7, pp. 5282–5291, Jul. 2018.

[33] S. Payami, R. K. Behera, A. Iqbal, and R. Al-Ammari, "Common-mode voltage and vibration mitigation of a five-phase three-level NPC inverter fed induction motor drive system," *IEEE J. Emerg. Sel. Topics Power Electron.*, vol. 3, no. 2, pp. 349–361, Jun. 2015.

Jiayao Li (Student Member, IEEE) received the M.S. degree in electrical engineering in 2020 from Southwest Jiaotong University, Chengdu, China, where he is currently working toward the Ph.D. degree in electrical engineering. His research interests include modeling, control, and modulation of permanent magnet synchronous motor drives.

Wensheng Song (Senior Member, IEEE) received the B.S. degree in electronic and information engineering and the Ph.D. degree in electrical engineering from Southwest Jiaotong University, Chengdu, China, in 2006 and 2011, respectively.

From September 2009 to September 2010, he was a Visiting Scholar with the Department of Electrical Engineering and Computer Science, University of California at Irvine, Irvine, CA, USA. From July 2015 to December 2015, he was a Visiting Scholar with the University of Alberta, Edmonton, AB, Canada. He is currently a Full Professor with the School of Electrical Engineering, Southwest Jiaotong University. His current research interests include power electronics, motor drives, railway traction drive systems, and multilevel converters.

Hao Yue (Student Member, IEEE) was born in China. He received the B.S. and M.S. degrees from the Henan Technology University, Jiaozuo, China, in 2018 and 2021, respectively. He is currently working toward the Ph.D. degree with Southwest Jiaotong University, Chengdu, China.

His current research interests include the design and control of high-power density converter, wide bandgap semiconductors, and their applications.

Na Sun was born in China. She received the B.S. degree in electrical engineering in 2021from the Southwest Jiaotong University, Chengdu, China, where she is currently working toward the M.S degree in electrical engineering.

Her current research interests include motor drives.

Chenwei Ma (Member, IEEE) was born in China. He received the Ph.D. degree in electromechanical engineering from Ghent University, Ghent, Belgium, in 2021.

Since 2021, he has been a Postdoctoral Researcher with the Department of Electromechanical, Systems and Metal Engineering, Ghent University. Since 2022, he has been with the Department of Electrical Engineering, Southwest Jiaotong University, Chengdu, China, where he is currently an Assistant Professor. His current research interests include motor drives, model predictive control and data-driven techniques applied to power converters and electric drives.

Rong Feng received the B.S. degree in electrical engineering from the Southwest University of Science and Technology, Mianyang, China, in 2021. He is currently working toward the M.S. degree in electrical engineering with Southwest Jiaotong University, Chengdu, China.

His current research interests include power electronics and motor drives.